High-contrast imaging of HD 29992 and HD 196385 with the Gemini Planet Imager

Luciano H. García [1]★ R. Petrucci [1,2] E. Jofré[1,2,3] and M. Gómez[1,2]

[1]*Universidad Nacional de Córdoba, Observatorio Astronómico de Córdoba, Laprida 854, X5000BGR Córdoba, Argentina*
[2]*Consejo Nacional de Investigaciones Científicas y Técnicas (CONICET), Godoy Cruz 2290, C1425FQB Buenos Aires, Argentina*
[3]*Instituto de Astronomía, Universidad Nacional Autónoma de México, Circuito Exterior, Ciudad Universitaria, 04510 Ciudad de México, México*

ABSTRACT

Based on high-contrast images obtained with the Gemini Planet Imager (GPI), we report the discovery of two point-like sources at angular separations $\rho \sim 0.18$ and 0.80 arcsec from the stars HD 29992 and HD 196385. A combined analysis of the new GPI observations and images from the literature indicates that the source close to HD 29992 could be a companion to the star. Concerning HD 196385, the small number of contaminants (~ 0.5) suggests that the detected source may be gravitationally bound to the star. For both systems, we discarded the presence of other potential companions with $m > 75$ M_{Jup} at $\rho \sim 0.3$–1.3 arcsec. From stellar model atmospheres and low-resolution GPI spectra, we derive masses of ~ 0.2–0.3 $M_\odot$ for these sources. Using a Markov-chain Monte Carlo approach, we performed a joint fit of the new astrometry measurements and published radial velocity data to characterize the possible orbits. For HD 196385B, the median dynamic mass is in agreement with that derived from model atmospheres, whilst for HD 29992B the orbital fit favours masses close to the brown dwarf regime (~ 0.08 $M_\odot$). HD 29992 and HD 196385 might be two new binary systems with M-type stellar companions. However, new high angular resolution images would help to confirm definitively whether the detected sources are gravitationally bound to their respective stars, and permit tighter constraints on the orbital parameters of both systems.

Key words: instrumentation: high angular resolution – techniques: imaging spectroscopy – binaries: visual – stars: imaging – stars: low-mass.

1 INTRODUCTION

The direct imaging technique has made possible the discovery of tens of wide ($a \geq 10$ au), low-mass companions ($m < 75$ M_{Jup}) that populate a little explored region of the mass versus orbital radius diagram (see Bowler 2016 for a review). Nevertheless, despite these findings, their occurrence rate is still uncertain (Launhardt et al. 2020). In addition, several imaged companions have been detected inside the gaps of debris discs, such as HR 2562B (Konopacky et al. 2016) and HD 193571B (Musso Barcucci et al. 2019), with these discoveries having challenged our current understanding about the formation and later evolution of these companions. Monitoring direct imaged companions allows their dynamic mass to be estimated (independent of the assumptions of evolutionary models), so they can be used as empirical benchmarks for evolutionary models, especially of low-mass objects (Franson et al. 2022). Hence, there is a need to increase the number of known systems with wide, low-mass companions, in order to provide a better estimate of the rate of occurrence and an improved understanding of the predominant mechanisms that shape such systems.

Direct imaging combined with coronagraphy is currently one of the most efficient techniques for searching for companions in wide orbits. Here, we used the Gemini Planet Imager (GPI) at Gemini South (Macintosh et al. 2014) to obtain high-contrast, high angular resolution coronagraphic images of two stars with evidence of wide, low-mass companions through radial velocity monitoring: HD 29992 and HD 196385. In this work, we report the discovery of two point-like sources in the high-contrast images of these stars obtained with GPI. In Section 2, we present the targets and briefly review previous studies that have searched for companions around both stars. The observations and the data reduction are described in Section 3. In Section 4 we investigate the companionship and characteristics of the detected sources. To put some initial constraints on the possible orbits, we use the package orbitize! to perform a joint fit of the new astrometry data from GPI and existing radial velocity measurements from the literature. Finally, in Section 5 we summarize the results and present our conclusions.

2 PROPERTIES OF THE TARGETS AND PREVIOUS SURVEYS FOR COMPANIONS

We selected the stars HD 29992 and HD 196385, because both have shown evidence of low-mass companions in wide orbits. Borgniet et al. (2017) studied the long-term variations of radial velocity (RV) of these stars, and for HD 29992 they found a quadratic RV trend over the ~ 4.8 year time baseline of their compiled data. Taking into account this time baseline and also the amplitude of the variations, the authors inferred the presence of a companion, most likely a low-mass star (despite them estimating a minimum mass of ~ 40 M_{Jup}) at

★ E-mail: luciano.garcia.030@unc.edu.ar

Table 1. Relevant parameters for the observed targets.

Target	V[a] (mag)	H[b] (mag)	d[c] (pc)	$\mu_\alpha \times \cos(\delta)$[c] (mas)	μ_δ[c] (mas)	SpT[a]	mass[d] ($M_\odot$)	Age[e] (Gyr)
HD 29992	5.1	4.3	28.8 ± 0.1	42.56 ± 0.06	212.70 ± 0.07	F3IV	1.47 ± 0.24	$1.7^{+0.2}_{-0.2}$
HD 196385	6.4	5.6	47.7 ± 0.1	73.04 ± 0.02	-16.41 ± 0.02	A9V	1.53 ± 0.27	$1.2^{+0.3}_{-0.7}$

Notes. [a]*SIMBAD* database.
[b]2MASS All Sky Catalog of point sources (Cutri et al. 2003).
[c]*GAIA* DR2 catalogue (Gaia Collaboration et al. 2018).
[d]Stassun et al. (2019).
[e]Casagrande et al. (2011).

a separation larger than 3 au. For HD 196385, Borgniet et al. (2017) reported a linear trend in the RV observations, but were not able to provide a limit on the separation or on the mass of a potential companion. Basic parameters of the stars are listed in Table 1.

Previous attempts to detect substellar mass companions around HD 29992 through high-contrast, high angular resolution images were carried out by Ehrenreich et al. (2010) using the Nasmyth Adaptive Optics System (NAOS) Near-Infrared Imager and Spectrograph (CONICA), known as NaCo, on the Very Large Telescope (VLT). These authors obtained direct and coronagraphic (with a focal plane mask of diameter ⌀ = 0.7 arcsec) images, but did not report any sources in the images and discarded the presence of companions with masses $m > 75$ M$_{\rm Jup}$ beyond ∼1.9 arcsec (∼55 au) from the central star. For HD 196385, we are not aware of any previous attempts to detect companions through high angular resolution images.

3 OBSERVATIONS AND DATA REDUCTION

High-contrast images and low-resolution spectra ($R \sim 45$) in the H band for any source in the field of view (FOV: ∼2.8 × 2.8 arcsec^2) around the selected stars HD 29992 and HD 196385 were obtained using the Integral Field Spectroscopy mode (IFS; spatial scale 14.13 mas per lenslet) of GPI in combination with a focal plane mask (FPM; diameter ⌀ = 246 mas). The observations for HD 29992 were executed in 2019 November, and 24 images were obtained for this target. HD 196385 was observed in 2019 September, but only four images were obtained (program GS-2019B-Q-107; PI: Luciano Héctor García). All the observations were carried out in the pupil-tracking mode[1] in order to apply the angular differential imaging (ADI) technique (Marois et al. 2006).

For processing the raw data and constructing three-dimensional (3D) wavelength-calibrated datacubes (x, y, λ), we used the GPI Data Reduction Pipeline[2] version 1.3.0 (DRP: Perrin et al. 2016). The usual primitives[3] were applied for subtracting the dark background, correcting for variations between the CCD readout channels and microphonics, interpolating over bad pixels, compensating for flexure, and converting from raw 2D IFS frames to 3D datacubes. Argon arc lamp exposures taken prior to the science exposure sequences were used for wavelength calibration and to determine the locations and fluxes of the four satellite spots created by the apodizer. The satellite spots were used for image registration. The limited number of images (and sky rotation) for HD 196385 did not allow us to process the images further to remove the Point Spread Function of the star and
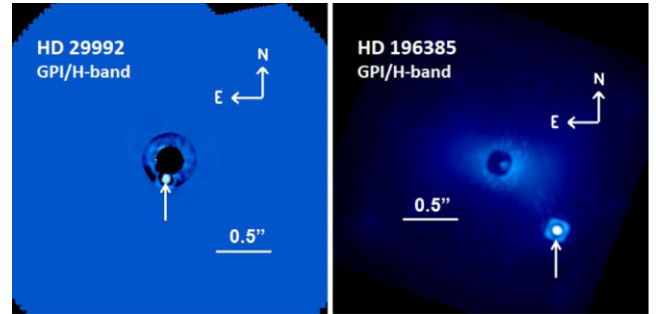
Figure 1. Left: ADI combination of the 24 images for HD 29992 using the KLIP algorithm. The wavelengths of the datacube are median-combined. A point-like source is clearly visible towards the south-east of the star. Right: median-combined image for one of the datacubes of HD 196385. The source at $\rho \sim 0.8$ arcsec from the star is distinctly present.

instrumental scattered light. However, in the case of HD 29992, it was possible to apply the Karhunen–Loève Image Projection (KLIP) algorithm provided by the PYTHON library pyKLIP[4] (Wang et al. 2015) to correct the final image for these effects. For the astrometric calibrations, we adopted a plate-scale of 14.166 ± 0.007 mas pixel^{-1} (Konopacky et al. 2014; De Rosa et al. 2015). This value is consistent with a more recent measurement of the pixel scale (14.161 ± 0.021 mas pixel^{-1}) obtained by De Rosa et al. (2020). The measured position angles (PAs) were adjusted by 0.45 ± 0.11 deg according to the updated north offset angle given by De Rosa et al. (2020), and we used the offset closest to the date of the observations from this study.

4 ANALYSIS AND RESULTS

Fig. 1 shows the GPI images for HD 29992 and HD 196385 after applying the reduction steps listed in Section 3. A point-like source is visible in the images of each star, with both sources being bright enough to be identifiable in the individual datacubes. The angular (ρ) and projected separations, plus PAs and measured contrasts (ΔH), are listed in Table 2. When processing the raw data, we also extracted the achieved contrast versus angular separation to the central star. In the case of HD 29992, the contrast was corrected from the throughput of the ADI algorithm, with the resulting curves shown in Fig. 2. We combined the contrast curves with models of atmospheres for substellar mass objects to obtain the approximate mass limits to the companions that could be detected in the images. Fig. 3 displays these resulting limits using the models from Baraffe et al. (2003). In addition to the mentioned sources, we can discard the presence

---

[1]In this mode, the FOV is allowed to rotate around the central star.
[2]Available at http://docs.planetimager.org/pipeline/.
[3]A primitive is the name that an elementary algorithm (to be applied on the files, for example, for removing the dark background or building the 3D datacubes) receives in the GPI-DRP.

[4]Available at https://pyklip.readthedocs.io/en/latest/index.html.

Table 2. Measured parameters for the newly detected sources.*

Target	ρ ($\times 10^{-3}$ arcsec)	Separation (au)	PA ($^\circ$)	ΔH (mag)
HD 29992B	175 ± 1	5.04 ± 0.04	168.1 ± 0.3	5.9 ± 0.5
HD 196385B	802 ± 1	38.3 ± 0.1	219.1 ± 0.2	4.9 ± 0.2

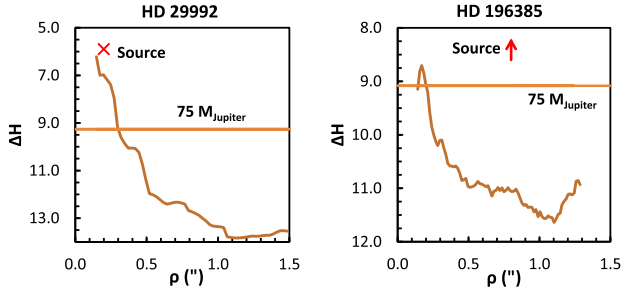*Notes.* *We are using the designations HD 29992B and HD 196385B for simplicity here.

Figure 2. Left: measured contrast curve (algorithm throughput corrected) for the final image of HD 29992. The horizontal line represents the contrast of a companion with a mass $m = 75\,M_{Jup}$ according to the models of Baraffe et al. (2003). The cross shows the location of the detected source. Right: measured contrast for HD 196385. The arrow indicates that the contrast of the detected source falls outside the range of the plot. The horizontal line represents the contrast of a 75 M_{Jup} companion.
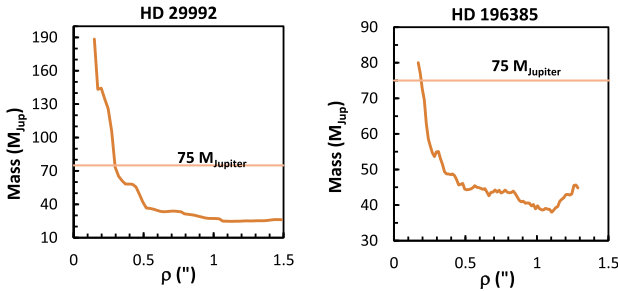

Figure 3. Mass limits calculated from combining the measured contrasts and the models of Baraffe et al. (2003). Any companion in the FOV of GPI with a mass above the curves would have been detected in the images. Horizontal lines indicate the location of a companion with mass $m \sim 75\,M_{Jup}$.

of companions with mass $m > 75\,M_{Jup}$ beyond $\rho \sim 0.3$ arcsec (~ 8 au) and $\rho \sim 0.2$ arcsec (~ 9 au) orbiting around HD 29992 and HD 196385, respectively. Also, by taking into account the results from Ehrenreich et al. (2010), it is possible to discard the presence of companions with $m > 75\,M_{Jup}$ between $\rho \sim 0.3$ and ~ 10 arcsec for HD 29992.

4.1 Association with the central star

The search for companions through images must address the possibility of a fortuitous alignment with stars projected in the FOV, especially for those at wide separations. A common practice is to use multi-epoch images for comparing the proper motion of a potential companion with that of the central star, in order to infer whether both are co-moving in the sky. However, GPI was unfortunately taken out of service during the first half of 2020, before we were able to obtain second-epoch images to measure the proper motions of the detected sources. Therefore, in this section, we discuss other ways
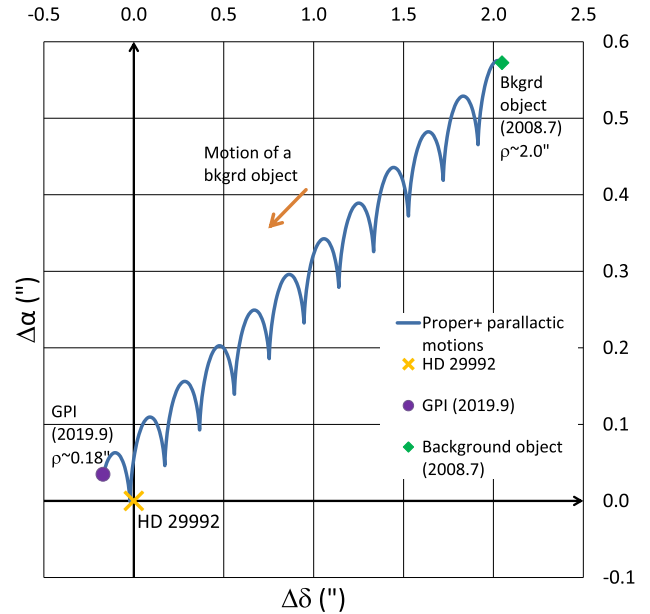

Figure 4. Relative position of the detected source with respect to HD 29992 (the cross at the origin of the coordinate system). The circle indicates its location in the GPI images (date =2019.9). The square is the calculated position at the date of the Ehrenreich et al. (2010) images (2008.7), assuming that the source is an infinitely distant object.

of examining whether the detected sources may be gravitationally bound to their respective central stars.

4.1.1 HD 29992

For HD 29992, it was possible to use the images from Ehrenreich et al. (2010) to evaluate the companionship of the source detected in the GPI images. By assuming that this is an infinitely distant object, we used the proper motion of the star and the position in the GPI images to calculate its approximate angular separation and position angle on the date (2008.7) of the images from Ehrenreich et al. (2010). We named this date Epoch 1. A background object will show an opposite drift in comparison with the proper motion of the star. The GPI images (Epoch 2 – 2019.9) are separated by just over 11 years from Epoch 1. This relatively large time baseline and the high proper motion of the star allowed us to ignore sources of error in the proper motion of the star and the measured position of the potential companion. At Epoch 1, we calculated that the approximate angular separation of the source would be $\rho \sim 2$ arcsec (PA $\sim 13.1^\circ$), assuming that this is an infinitely distant object. This is illustrated in Fig. 4. An object with the contrast observed in the GPI images, located at $\rho \sim 2$ arcsec from HD 29992 in Epoch 1, should have been detected in the Ehrenreich et al. (2010) images. This lack of detection suggests that the source is co-moving with the star and that it was hidden by the FPM, or fell within the glare of the central star in the Ehrenreich et al. (2010) images.

As mentioned in Section 2, Borgniet et al. (2017) estimated that a companion around HD 29992 must be located at a separation larger than 3 au, and is most likely a low-mass star. This is in good agreement with the separation measured from the GPI images (~ 5 au) and the estimated mass of $m \sim 0.2\,M_\odot$ (see Sections 4.2 and 4.3). To address the question of whether the Borgniet et al. (2017) observations could have detected the source seen in the GPI images, we calculated the inclination $i_\star$ of the system. To carry this out, it

Table 3. Adopted luminosity function.

SpT	M_H (mag)	Number (pc^3 (SpT)$^{-1}$ × 1 × 10^3)	SpT	M_H (mag)	Number (pc^3 (SpT)$^{-1}$ × 1 × 10^3)
B8	0.1	0.04	K2	4.4	3.10
A0	0.6	0.30	K4	4.6	2.50
A2	1.2	0.40	K5	4.6	2.50
A5	1.5	0.50	K7	4.9	4.50
A7	1.7	0.50	M0	5.4	5.00
F0	2.0	0.70	M1	5.7	5.00
F2	2.2	0.70	M2	6.1	5.20
F5	2.7	0.80	M3	6.7	11.00
F8	3.1	1.50	M4	7.5	9.50
G0	3.3	1.90	M5	8.5	7.00
G2	3.4	1.90	M6	9.5	5.00
G5	3.6	1.90	M7	10.1	3.00
G8	3.9	2.60	M8	10.5	2.00
K0	4.1	2.60	M9	10.7	2.00

was necessary to determine the rotation period of the star for the first time. We used data from the *Transiting Exoplanet Survey Satellite* (*TESS*: Ricker 2015). The details of this calculation are presented in Appendix A. The value obtained for $i_\star$ was ∼65.3°. According to the sensitivity limits from Borgniet et al. (2017, see fig. 9 from their work) and the resulting $i_\star$, a companion with a mass of $m \sim 0.2$ M$_\odot$ located at ∼5 au from the star should have been detected in their observations. In addition, there is no evidence for other companions, pointing to the source detected in the images with GPI as being the possible origin for the trend observed in the RV of the star. Therefore, the trend found by Borgniet et al. (2017), plus the first-epoch observations from Ehrenreich et al. (2010), leads us to propose that the source in the images of HD 29992 is gravitationally bound to the star.

4.1.2 HD 196385

For HD 196385, we used statistical arguments to evaluate the chances of finding a field star in the images with GPI by considering how many B8–M9 type stars would be expected in the GPI FOV. The Spectral Types (SpT) taken into account were limited to those that contributed the most to the number of potential contaminants due to their spatial density and detection distances. The calculation requires knowledge of the volume density and luminosity of the field stars. We assumed an isotropic distribution and neglected the decrease of volume density with increasing distance from the Galactic plane, although this approximation will overestimate the number of potential contaminants. For the luminosity function, we combined the results in the *J* band from Cruz et al. (2003) and Reid et al. (2004). Also, the magnitude–SpT relation from Kraus & Hillenbrand (2007) and the absolute magnitudes from Kirkpatrick et al. (2012) were used to calculate the corresponding *H*-band luminosity function.

Next, we calculated the maximum distances at which our images may detect each spectral type, assuming a uniform sensitivity between $\rho \sim 0.1$ arcsec (at the edge of the FPM) and the angular separation of the detected source, and using the highest sensitivity achieved in the images of each target. By making this approximation, we are overestimating the capability to detect potential contaminants. Then, the corresponding volume was calculated and multiplied by the density listed in Table 3. By adding the results from all the spectral types in Table 3, we found a total of ∼0.5 objects per GPI field. It is worth mentioning that the actual number of contaminants is likely to

Table 4. Absolute magnitude, mass, and effective temperature of the detected sources.

Target	M_H (mag)	Mass (M$_\odot$)	T_{eff} (K)
HD 29992B	7.9 ± 0.6	0.19 ± 0.05	3593 ± 160
HD 196385B	7.1 ± 0.2	0.28 ± 0.03	3790 ± 24

be smaller than the one calculated here, as we have not only ignored the decrease in density when moving away from the Galactic plane, but also optimized the ability to detect contaminants by using the maximum sensitivity for all angular distances.

To check the result obtained by this simple method, we simulated a field using the area covered by GPI (∼7 × 10^{-7} deg^2) centred on the Galactic coordinates of HD 196385 ($l = 293.1°$, $b = -33.7°$) using the TRILEGAL Galactic model online tool[5] (Girardi et al. 2012). Default parameters were used for the bulge, halo, and thin/thick discs, and the lognormal initial mass function from Chabrier (2001) was used. The limiting magnitude in the *H* band was set to ∼17, according to the contrast achieved. Then the number of objects calculated by the tool was zero, most likely due to the extremely small area covered by GPI. Thus, the low number of expected contaminants per image suggests that the chance of a fortuitous alignment is rather low, and that the detected source may be an actual companion to HD 196385.

Borgniet et al. (2017) also studied the long-term RV variations of HD 196385. Following the same procedure as with HD 29992, we calculated the rotation period of HD 196385 for the first time using *TESS* photometry, obtaining $i_\star \sim 16.9°$. A companion with $m \sim 0.3$ M$_\odot$ (see Section 4.2), at ∼38 au from the star, could not have been detected in the observations of Borgniet et al. (2017, see fig. 9 from their work). However, the authors reported a linear trend in the radial velocity that could have been due to a companion to HD 196385, but they were not able to estimate a limit for its mass or separation. Therefore, it is difficult to validate whether this companion corresponded to the source identified in the GPI images.

4.2 Determination of spectral types for the companion stars

In Table 4, we list the absolute magnitudes (M_H) assuming that the detected sources are gravitationally bound to their respective central stars, which are outside the range covered by the models of Baraffe et al. (2003). Therefore, we used the isochrones from Girardi et al. (2000) for low- and intermediate-mass stars. Adopting the same ages for the companions as those for the central stars, we applied the Girardi et al. (2000) models to derive the masses. Table 4 lists these masses, as well as the effective temperature of the detected companions to HD 29992 and HD 196385. These results are compatible with M-type stars.

We also extracted the *H*-band observed spectra of the detected sources in order to compare the overall shape of these with those of known objects in the SpeX Prism Spectral (Burgasser 2014) and NIRSPEC Brown Dwarf Spectroscopic Survey (NIRSPEC BDSS: McLean et al. 2003) libraries. This allowed us to use another method of characterizing the detected sources, independent of the analysis with models of stellar atmospheres.

To perform the comparison, we wrote a routine that calculates the value of a parameter χ^2, defined as $\chi^2 = (F_{\lambda,\text{GPI}} - F_{\lambda,\text{lib}})^2/(\sigma_{\lambda,\text{GPI}}^2 + \sigma_{\lambda,\text{lib}}^2)$. Here, $F_{\lambda,\text{GPI}}$ and $F_{\lambda,\text{lib}}$ are the fluxes of the GPI and the library spectra, respectively, at wavelength λ, with $\sigma_{\lambda,\text{GPI}}$, and $\sigma_{\lambda,\text{lib}}$ the

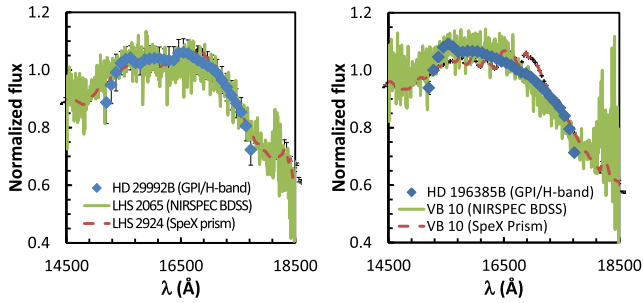[5]Available at http://stev.oapd.inaf.it/cgi-bin/trilegal.

Figure 5. *H*-band spectra for HD 29992B (left panel) and HD 196385B (right panel) from the GPI observations (blue squares). The dashed line represents the best match of the SpeX Prism Spectral Libraries to the GPI data. The continuum solid line corresponds to the NIRSPEC BDSS library.

errors in the fluxes. Before calculating χ^2, the library spectra were degraded to the resolution of GPI by convolving with a Gaussian kernel, after which they were normalized along with the GPI spectra. We cut off the wavelengths at both ends of the GPI spectra, since these regions can be affected by filter transmission and the process of microspectra extraction. Each GPI spectrum was compared with each library spectrum to derive the best match with the smallest χ^2.

Fig. 5 shows the extracted spectra from the GPI observations, together with the best-matching spectrum from the libraries cited above. For HD 29992B, the two M9V stars LHS 2924 (SpeX prim) and LHS 2965 (NIRSPEC BDSS) provided the matches with the minimum residuals. In the case of HD 196385B, both libraries gave the same best match, namely the M8-type star VB 10. Therefore, the GPI *H*-band spectra suggest an M spectral type for both detected companions. Although some caution is advised regarding the results of this analysis (given the small wavelength range and spectral resolution of the data from GPI), they are compatible with those obtained using models of stellar atmospheres.

4.3 Orbit fitting

To obtain a preliminary characterization of the orbits of the companions, we performed a join fit of the astrometry data from GPI (in Table 2) and the public RV measurements available from the instrument High Accuracy Radial velocity Planet Searcher (HARPS: Trifonov et al. 2020), with the RV values being listed in Table 5. We then used the PYTHON package orbitize![6] (Blunt et al. 2020), designed to compute posterior distributions of orbital elements for data covering short fractions of the orbit. The orbitize! package implements the Bayesian rejection sampling algorithm Orbits For The Impatient (OFTI: Blunt et al. 2017) and the ptemcee parallel-tempered Markov-chain Monte Carlo (MCMC) approach to sampling posterior distributions from Foreman-Mackey et al. (2013). In the present study, the parallel-tempered algorithm ptemcee (Vousden, Farr & Mandel 2016) was applied. In addition to the RV and astrometry data, we adopted the distances and masses listed in Table 1.

We fitted six Keplerian elements (semimajor axis *a*, eccentricity *e*, inclination of the orbit *i*, argument of periastron ω, position angle of nodes Ω, and epoch of periastron τ), plus the mass of the companion (m_{sec}). Hereafter, we will refer to this as the 'dynamical' mass. Using the stellar mass, the dynamical mass, and the semimajor axis

[6]Available at https://github.com/sblunt/orbitize.

Table 5. RV measurements used in the orbit fitting.

	HD 29992			HD 196385	
BJD	RV (m s⁻¹)	σ (m s⁻¹)	BJD	RV (m s⁻¹)	σ (m s⁻¹)
2453806.51	−727	6	2453875.82	−56	2
2453806.51	−606	5	2453875.83	−56	3
2453806.53	−675	5	2453875.89	−60	3
2453806.54	−512	5	2453875.90	−72	4
2453807.53	−716	6	2453880.82	−64	3
2453807.53	−696	6	2453880.82	−67	3
2453989.81	−252	5	2453881.83	−31	3
2453989.82	−317	5	2453881.83	−24	3
2454439.73	272	6	2453986.75	−59	3
2454439.73	186	8	2453986.76	−55	2
2454444.71	124	5	2454439.54	−42	3
2454444.71	78	5	2454439.55	−39	3
2454563.47	629	5	2454440.55	−5	2
2454563.48	452	5	2454440.56	−3	3
2454742.84	297	12	2454444.53	−41	3
2454742.85	175	8	2454444.54	−37	3
2454746.89	190	5	2455147.56	11	2
2454746.90	80	5	2455147.57	6	2
2454759.76	92	5	2455148.56	−19	2
2454759.76	121	5	2455148.57	29	2
2454763.74	141	5	2455150.55	−24	2
2454763.75	117	5	2455150.56	−16	2
2454774.77	319	5	2455385.85	10	2
2454774.77	428	5	2455385.86	4	2
2455147.71	151	7	2455386.81	−10	2
2455147.71	251	6	2455386.82	98	1
2455172.70	−74	6	2455386.82	−14	2
2455172.70	180	7	2455386.83	−5	2
2455384.94	330	8	2455386.84	−18	2
2455565.59	285	6	2455386.84	−7	2
2455565.59	143	6	2455386.85	−4	2
2455568.58	242	4	2455386.86	21	2
2455568.58	207	5	2455724.85	40	2
2455596.57	−258	4	2455724.86	39	2
2455596.58	−180	8	2455726.75	13	2
			2455726.75	8	2
			2455726.76	−5	2
			2455726.77	−4	2
			2455726.78	−3	2
			2455726.78	−7	2
			2455726.79	−2	2
			2455726.80	−10	2
			2455726.81	−11	2
			2455726.81	−14	2
			2455726.82	−15	2
			2455763.76	22	2
			2455763.77	14	2
			2455763.78	11	2
			2455763.80	−1	2
			2455763.81	2	2
			2455763.82	−4	2
			2455763.83	−4	2
			2455763.84	−11	2
			2455764.85	22	2
			2455764.86	18	2
			2455765.85	1	2
			2455765.86	66	3

Table 6. Results for the orbits of HD 29992B.

Orbital element	Prior range	Prior distribution	Best	Median	68% confidence range	95% confidence range
a (au)	10^{-3}–10^4	Uniform in log a	4.6	4.7	4.6–4.9	4.5–5.1
e	0.0–1.0	Uniform in e	0.6	0.5	0.4–0.6	0.4–0.7
i (°)	0–180	Uniform in sin i	153	117	20–161	8–173
$0 \leq i < 90$ (°)	...	...	...	27	13–41	6–55
$90 \leq i < 180$ (°)	...	...	...	153	134–168	117–174
ω (°)	0–360	Uniform in ω	38	37	32–43	26–53
Ω (°)	0–360	Uniform in Ω	151	61	55–280	30–299
$0 \leq \Omega < 180$ (°)	...	...	...	64	44–75	26–166
$180 \leq \Omega < 360$ (°)	...	...	...	274	263–288	256–305
τ	0.0–1.0	Uniform in τ	0.6	0.6	0.2–0.8	0.0–1.0
m_{sec} (M$_\odot$)	10^{-2}–2	Uniform in log m_{sec}	0.08	0.08	0.05–0.18	0.04–0.4
P (yr)	...	...	7.5	7.7	7.5–8.1	7.4–8.7
Log(likelihood)	...	...	−81	-6.2×10^4	...	...

Table 7. Results for the orbits of HD 196385B.

Orbital element	Prior range	Prior distribution	Best	Median	68% confidence range	95% confidence range
a (au)	10^{-3}–10^4	Uniform in log a	33	36	33–40	30–45
e	0.0–1.0	Uniform in e	0.6	0.5	0.4–0.6	0.3–0.8
i (°)	0–180	Uniform in sin i	46	66	52–83	36–105
ω (°)	0–360	Uniform in ω	259	231	211–251	193–278
Ω (°)	0–360	Uniform in Ω	147	193	171–212	144–232
τ	0.0–1.0	Uniform in τ	0.6	0.5	0.4–0.5	0.3–0.7
m_{sec} (M$_\odot$)	10^{-6}–2	Uniform in log m_{sec}	0.26	0.30	0.25–0.36	0.20–0.44
P (yr)	...	...	151	161	141–186	124–223
Log(likelihood)	...	...	137	53	...	...

values of each walker at each accepted iteration, we calculated the corresponding orbital period (P).

Tables 6 and 7 show a summary of the orbital parameters, their prior distributions, ranges, and also the results of the orbital fitting. In the following discussion, we adopt the median values of the marginalized posterior distributions as being a representative estimator of each parameter's value, and the 68 per cent confidence intervals as the errors. For comparison, column 'Best' lists the results for the orbit with the highest value of log(likelihood)[7] in our runs. The corresponding log(likelihood) values for both sets of orbital parameters are also presented in Tables 6 and 7.

4.3.1 HD 29992

For HD 29992, we performed several initial tests varying the number of required accepted orbits and burn-in steps. Finally, we required 1 000 000 accepted orbits for building the posterior distributions. The MCMC sampler was run for 1000 steps using 1000 walkers at each of the 20 temperatures after 26 500 steps of burn-in, in order to allow the walkers to converge. Median values, together with the 68 and 95 per cent confidence ranges for each parameter, are listed in Table 6, and Fig. 6 shows a plot of 50 accepted orbits selected randomly.

The median for the distribution of the semimajor axis is $4.7^{+0.2}_{-0.1}$ au, with the corresponding median for the period distribution being $7.7^{+0.4}_{-0.2}$ yr. Our fit constrains the semimajor axis for the possible orbits tightly. This value is close to the projected separation measured in the images ($\sim$5 au). For the eccentricity, the fit seemed to favour orbits
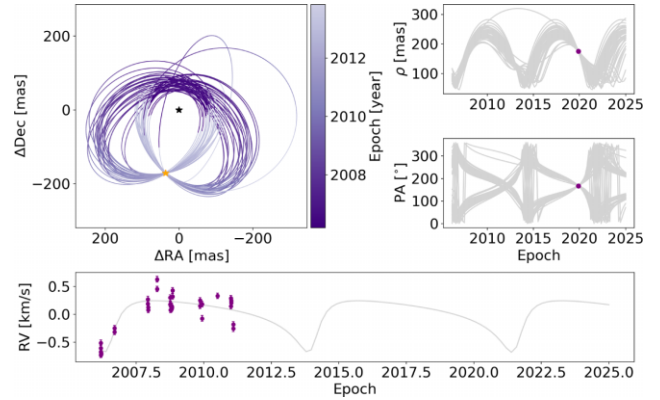

Figure 6. Left upper panel: plot of 50 accepted orbits selected randomly for HD 29992. The black star indicates the position of the primary component, while the orange star is the location of the companion. Right panels: the same orbits as above (in grey) in a diagram of separation and PA versus epoch. The purple stars are measurements with GPI. Bottom panel: RV time series for the primary star. The light blue dots are the RV measurements from HARPS. The solid grey line is the best fit found with `orbitize!`.

with relatively high eccentricities, with the median being $0.5^{+0.1}_{-0.1}$ and values as high as $e \sim 0.7$ at the 95 per cent confidence level.

The orbit inclination (i) is not very well constrained by our fit. The distribution in Fig. 7 reveals two separate clusters of accepted orbits around $i \sim 27°$ and $i \sim 153°$. In this case, the median is not a good reference value. Table 6 lists the medians and confidence ranges for orbits with $0 \leq i < 90°$ and $90 \leq i < 180°$. Both sets of orbits are closer to the plane of the sky than to an edge-on configuration ($i \sim 90°$) and produce RV curves of similar characteristics. The difference is
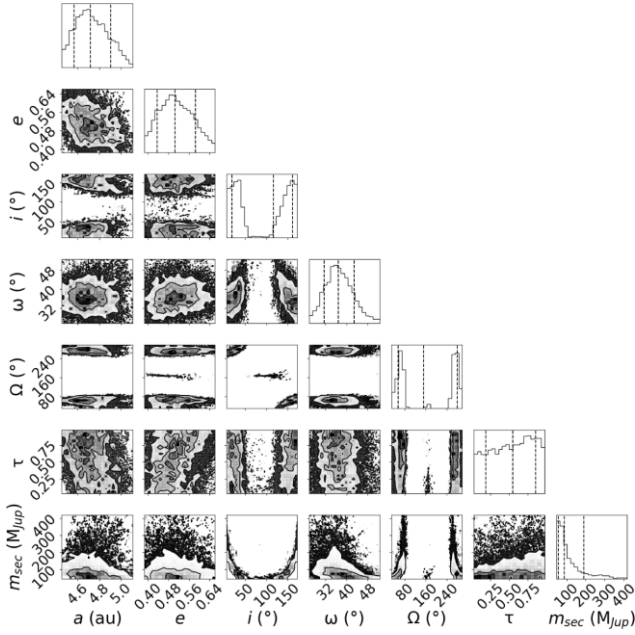
---

[7]The parameter log(likelihood) is a measure of the goodness of our fits: the larger the log(likelihood), the better the fit to the observational data.

Figure 7. Posterior and joint distributions built using 10^6 accepted orbits for HD 29992B. The vertical dashed lines indicate the 16th, 50th, and 84th percentile values. For clarity, the panels show only 95 per cent of the samples.
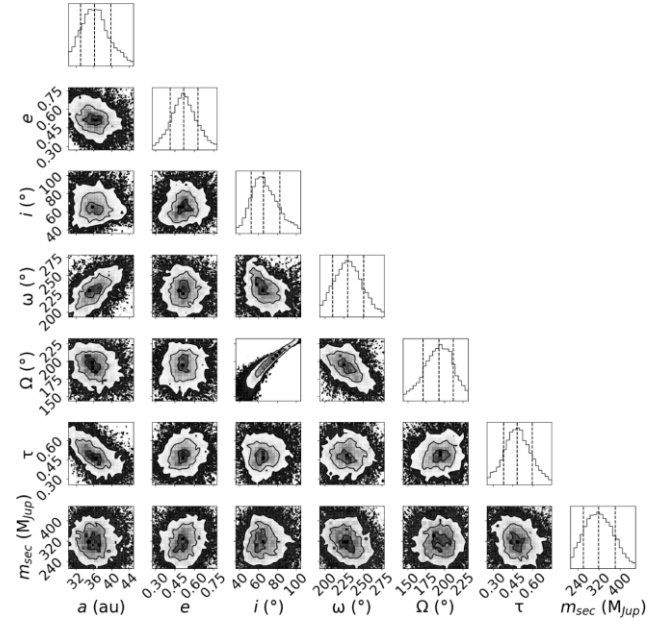

Figure 8. Posterior and joint distributions for the fitted parameters for HD 196385B. The vertical dashed lines indicate the 16th, 50th, and 84th percentile values. The one-dimensional distribution of each element is shown on the diagonal. For clarity, the panels show only 95 per cent of the samples.

that for orbits of $0 \leq i < 90°$ the companion orbits counterclockwise in the sky (north is up, east left), while for inclinations of $90 < i \leq 180°$ the motion is clockwise. In either case, neither of the orbits is coplanar with the equatorial plane of the central star ($i_\star \sim 65.3°$). However, low-inclination orbits are consistent with a low-mass star companion. If this was not the case, then larger amplitudes for the RVs would be expected.

The argument of periastron (ω) is relatively constrained with a median value of $37^{+6}_{-5}°$. On the other hand, the position angle of the nodes (Ω) is poorly constrained by our fit and reveals a similar behaviour to the inclination angle, with a large number of orbits found with $\Omega \sim 64°$ and $\Omega \sim 274°$ (which is apparent from the random orbits plotted in Fig. 6). Table 6 lists the medians and confidence ranges for orbits with $0 \leq \Omega < 180°$ and $180 \leq \Omega < 360°$. This behaviour may be due to the fact that only one separation for a given date is available (Ω has no effect on the resulting RV curve), making it hard to know the orientation of the line of nodes on the plane of the sky. Additional measurements of separation and PA at different epochs would help to constrain the range of possible Ω values better.

For the dynamical mass of the companion, the median value is $0.08^{+0.10}_{-0.03}$ M$_\odot$. The fit favoured smaller masses than the one estimated using stellar atmosphere models (~ 0.19 M$_\odot$) and was closer to the brown dwarf regime. However, the distribution of m_{sec} in Fig. 7 contains many accepted orbits for objects with dynamical mass > 0.1 M$_\odot$ and values as high as ~ 0.4 M$_\odot$ at the 95 per cent confidence level.

In general, we found a good agreement between the parameters of the orbit constructed from the median values and the orbit with the highest probability in our run (i.e. highest log(likelihood)). The exceptions are the inclination i and the position angle of nodes Ω, which show a bimodal behaviour in their distributions. The median value is not a good reference value in these cases and the orbit constructed from the median values has a significantly lower log(likelihood) than our orbit with the highest probability. Moreover, the orbital fits are consistent with the astrometry data points of

separation, position angle (right panels in Fig. 6), and radial velocity (lower panel in Fig. 6). The relatively small amplitude observed in the RV data may have favoured the orbits of objects with smaller dynamic masses than those estimated using atmospheric models. On the other hand, the two clusters of orbits found around $i \sim 27°$ and $i \sim 153°$ agree better with the presence of a low-mass star companion. Fig. 6 shows that the RV grows from ~ -0.7 km s^{-1} to $\sim +0.4$–0.6 km s^{-1} at around 2007.5 before starting to decrease slowly again at later dates, but never reaching the minimum values initially detected. Therefore, it is not possible from these data to infer whether the RV could have smaller values (these data extend to about 60 per cent of the median orbital period). New observations of RV would be required to be able to put stronger constraints on the dynamical mass.

4.3.2 HD 196385

For HD 196385, we ran an initial test to obtain 1000 000 accepted orbits in the same way as that described above for HD 29992. Then, we used the results from this run to define the starting position of the 1000 walkers to obtain, once again, 1000 000 accepted orbits, but now with 100 burn-in steps. The median values from the first run, did not differ significantly from those obtained in the second run. We proceeded in this way to improve the fit over the RV data. The results are presented in Table 7. Posteriors and joint distributions are shown in Fig. 8, while Fig. 9 shows a plot of 50 random accepted orbits.

We found a median semimajor axis of 36 au, with 68 per cent confidence between 33 and 40 au, and a corresponding period of 161 years, with 68 per cent confidence between 141 and 186 years. The measured projected separation from the images (~ 38 au), albeit larger than the median value, is within the 68 per cent confidence level. The median eccentricity is $0.5^{+0.1}_{-0.1}$, with values as high as 0.8 at the 95 per cent confidence level, suggesting rather highly eccentric orbits for HD 196385B.
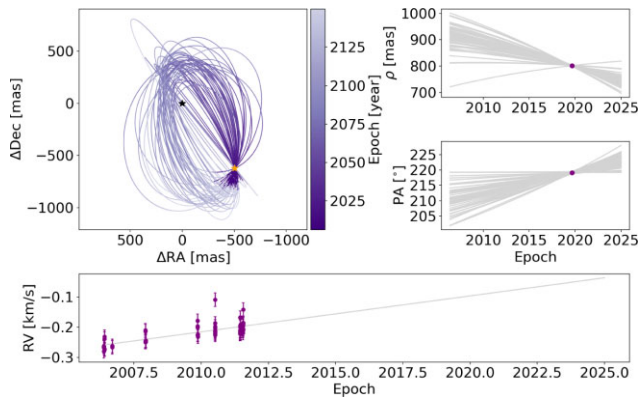
Figure 9. Left upper panel: plot of 50 accepted orbits selected randomly. The black and orange stars indicate the position of the primary component and the companion, respectively. Right panels: the same orbits as above (in grey) in a diagram of separation and PA versus time. The purple stars represent the measurements with GPI. Bottom panel: RV time series for the primary star. The light blue dots are the RV measurements from HARPS. The solid grey line is the best fit from `orbitize!`.

For the inclination, we obtained a median value of $i \sim 66°$. The distribution of i in Fig. 8 revealed a relatively broad range of inclinations, with values between $\sim 52°$ and $\sim 83°$ at 68 per cent confidence level. It is worth mentioning, however, that this range does not include edge-on orbits and suggests that the orbit of HD 196385B would not be coplanar with the equatorial plane of the star ($i_\star \sim 17°$). The argument of periastron ω and the position angle of the nodes Ω are both poorly constrained by our fit. For ω and Ω, the medians found are $231°^{+20}_{-20}$ and $193°^{+19}_{-22}$, respectively. Finally, the median dynamical mass of $0.30^{+0.06}_{-0.05}\,M_\odot$ found is in good agreement with the mass derived from the photometry and the stellar atmosphere models.

For HD 196385, Fig. 9 shows that the orbital fits are consistent with the measurements of separation, position angle (right panels in Fig. 9), and measured radial velocity (lower panel in Fig. 9). The median semimajor axis is in good agreement with the projected separation measured in the images, as well as the median dynamical mass, in comparison with the value derived from the atmosphere models. The parameters for the best orbit and those corresponding to the median orbit are within the 68 per cent confidence range. However, the position angle of nodes Ω, the argument of periastron ω, and the inclination i have a larger discrepancy. For Ω this is expected, because this parameter is not well constrained with only one measurement of separation and position angle. Radial velocity measurements show a gradual increase in velocity. However, the observations do not extend far enough in time[8] to determine a maximum or minimum value that would help place stronger constraints on ω and i. Given the long period inferred for this system, further astrometric measurements of separation and position angle would be particularly useful in narrowing down the set of possible orbits for HD 196385B.

5 SUMMARY AND CONCLUSIONS

We report the detection of two point-like sources at angular separations of $\rho \sim 0.18$ and ~ 0.80 arcsec from the stars HD 29992 and HD 196385, respectively. The combined analysis of the new

---

[8]RV data cover ~ 3 per cent of the 161-year period, or 5.2 years.

GPI observations and previous high spatial resolution images from Ehrenreich et al. (2010) suggests that the source detected close to HD 29992 is gravitationally bound to the star. The measured projected separation (~ 5 au) and estimated mass ($\sim 0.2\,M_\odot$) determined using models of stellar atmospheres are in good agreement with the characteristics predicted by Borgniet et al. (2017) from their analysis of RV measurements of the star. Moreover, we can discard the presence of additional companions with $m > 75\,M_{Jup}$ between $\rho \sim 0.3$ and ~ 1.5 arcsec from HD 29992.

For HD 196385, we used statistical arguments to evaluate the companionship of the detected source, and found that about ~ 0.5 objects would be expected in the GPI images. This suggests that the chances of a fortuitous alignment with a background star are rather low and that the detected source may be gravitationally bound to HD 196385. In that case, the companion would have a mass of $\sim 0.3\,M_\odot$ according to the models of stellar atmospheres. In addition, the contrast achieved in the individual datacubes allows us to rule out any potential companions with $m > 75\,M_{Jup}$ between $\rho \sim 0.2$ and ~ 1.3 arcsec.

We extracted and compared the observed *H*-band spectra of the detected sources with those of previously known objects. In both cases, we found that the best matches for the observed spectra were those of late M-type stars. This is roughly in agreement with the inferred masses using theoretical models of stellar atmospheres.

Using the PYTHON package `orbitize!`, we performed a joint fit of the new GPI astrometry data and previously existing RV measurements to infer the most likely orbits for HD 29992B and HD 196385B. For both systems, we found a good agreement between the projected separation measured in the images and the median semimajor axis of the posterior distributions. For HD 196385B, the median dynamical mass is also in good agreement with the mass estimated using the stellar atmosphere models. For HD 29992B, the orbital solutions favoured a dynamic mass (median of $0.08\,M_\odot$) closer to the brown dwarf regime than that estimated using models of stellar atmospheres ($0.2\,M_\odot$). The small dynamical mass is hard to reconcile with the high brightness observed in the GPI images (assuming that the source is at the distance of HD 29992). One possible explanation for this is that the inclination (i) of the orbit is low. As the posterior distribution of i for HD 29992B shows two clusters of accepted orbits with $i \sim 27°$ and $i \sim 153°$, this can explain the relatively low amplitude observed in the RV curve and is compatible with the mass estimated using stellar atmosphere models and the prediction from Borgniet et al. (2017).

Our analysis suggests that HD 29992 and HD 196385 could be two binary systems with an M-type secondary component orbiting at separations of ~ 5 and ~ 38 au, respectively, in relatively low-inclination orbits. However, new images are required to measure the proper motion of the detected sources and to confirm definitely whether they are co-moving with the central star. In addition, these images would help to put stronger constraints on the characteristics of both systems, in particular in the case of HD 29992.

Ciência, Tecnologia, Inovações e Comunicações (Brazil), and Korea Astronomy and Space Science Institute (Republic of Korea).

DATA AVAILABILITY

The data in this article are available from the Gemini Observatory Archive (https://archive.gemini.edu) with programme ID GS-2019B-Q-107. The data products generated from the raw data are available upon request to the author.

REFERENCES

Astropy Collaboration, 2013, A&A, 558, A33
Baraffe I., Chabrier G., Barman T. S., Allard F., Hauschildt P. H., 2003, A&A, 402, 701
Barnes S. A., 2007, ApJ, 669, 1167
Blunt S. et al., 2017, AJ, 153, 229
Blunt S. et al., 2020, AJ, 159, 89
Borgniet S., Lagrange A.-M., Meunier N., Galland F., 2017, A&A, 599, A57
Bowler B. P., 2016, PASP, 128, 102001
Burgasser A. J., 2014, in Singh H. P., Prugniel P., Vauglin I., eds, International Workshop on Stellar Spectral Libraries ASI Conference Series, 2014, Vol. 11, The SpeX Prism Library: 1000+ low-resolution, near-infrared spectra of ultracool M, L, T and Y dwarfs. p. 7
Casagrande L., Schönrich R., Asplund M., Cassisi S., Ramírez I., Meléndez J., Bensby T., Feltzing S., 2011, A&A, 530, A138
Chabrier G., 2001, ApJ, 554, 1274
Chowdhury S., Joshi S., Engelbrecht C. A., De Cat P., Joshi Y. C., Paul K. T., 2018, Ap&SS, 363, 260
Cruz K. L., Reid I. N., Liebert J., Kirkpatrick J. D., Lowrance P. J., 2003, AJ, 126, 2421
Cutri R. M. et al., 2003, VizieR Online Data Catalog. p. II/246
De Rosa R. J. et al., 2015, ApJ, 814, L3
De Rosa R. J. et al., 2020, Journal of Astronomical Telescopes, Instruments, and Systems, 6, 015006
Ehrenreich D., Lagrange A.-M., Montagnier G., Chauvin G., Galland F., Beuzit J.-L., Rameau J., 2010, A&A, 523, A73
Foreman-Mackey D., Hogg D. W., Lang D., Goodman J., 2013, PASP, 125, 306
Franson K., Bowler B. P., Brandt T. D., Dupuy T. J., Tran Q. H., Brandt G. M., Li Y., Kraus A. L., 2022, AJ, 163, 50
Gaia Collaboration, 2016, A&A, 595, A1
Gaia Collaboration, 2018, A&A, 616, A1
Girardi L., Bressan A., Bertelli G., Chiosi C., 2000, A&AS, 141, 371
Girardi L. et al., 2012, Astrophysics and Space Science Proceedings, 26, 165
Jenkins J. M. et al., 2016, Proc. SPIE, 9913, 99133E
Kirkpatrick J. D. et al., 2012, ApJ, 753, 156
Konopacky Q. M. et al., 2014, Proc. SPIE, 9147, 914784
Konopacky Q. M. et al., 2016, ApJ, 829, L4
Kraus A. L., Hillenbrand L. A., 2007, AJ, 134, 2340
Launhardt R. et al., 2020, A&A, 635, A162
Lightkurve Collaboration et al., 2018, Astrophysics Source Code Library, record ascl:1812.013
Macintosh B. et al., 2014, Proceedings of the National Academy of Science, 111, 12661
Marois C., Lafrenière D., Doyon R., Macintosh B., Nadeau D., 2006, ApJ, 641, 556
McLean I. S., McGovern M. R., Burgasser A. J., Kirkpatrick J. D., Prato L., Kim S. S., 2003, ApJ, 596, 561
Meibom S., Mathieu R. D., Stassun K. G., 2009, ApJ, 695, 679
Musso Barcucci A. et al., 2019, A&A, 627, A77
Perrin M. D. et al., 2016, Proc. SPIE, 9908, 1010
Reid I. N. et al., 2004, AJ, 128, 463
Ricker G. R. et al., 2015, J. Astron. Telesc. Instrum. Syst., 1, 014003
Scargle J. D., 1982, ApJ, 263, 835
Skumanich A., 1972, ApJ, 171, 565
Stassun K. G. et al., 2019, AJ, 158, 138
Trifonov T., Tal-Or L., Zechmeister M., Kaminski A., Zucker S., Mazeh T., 2020, A&A, 636, A74
Vousden W. D., Farr W. M., Mandel I., 2016, MNRAS, 455, 1919
Wang J. J., Ruffio J.-B., De Rosa R. J., Aguilar J., Wolff S. G., Pueyo L., 2015, Astrophysics Source Code Library, record ascl:1506.001

APPENDIX: CALCULATION OF THE INCLINATIONS FROM *TESS* DATA

We estimated the inclination ($i_\star$) of HD 29992 and HD 196385 using the classical equation:

$$i_\star = \sin^{-1} \frac{P_{\rm rot} \times v \sin(i_\star)}{2\pi R_\star}, \tag{A1}$$

where $P_{\rm rot}$ is the rotation period, $v \sin(i_\star)$ the projected rotational velocity, and $R_\star$ the radius of the star.

Rotation periods were determined from the two-minute cadence data provided by *TESS* (Ricker 2015). We used the tools available in the Lightkurve PYTHON package (Lightkurve Collaboration et al. 2018) to retrieve and analyse the Presearch Data Conditioning Simple Aperture Photometry (PDC_SAP), processed with the *TESS* Science Processing Operations Center (SPOC) pipeline (Jenkins et al. 2016). HD 29992 (TIC 77288515) was observed by *TESS* in sectors 4–5 (2018 October 18–December 11) and 31–32 (2020 October 21–December 17). However, given that all data from sector 4 and those at the end of sector 5 between 2458464.0 and 2458465.0 Barycentric Julian Date (BJD) were severely affected by systematics, we did not use them for further analysis. For HD 196385 (TIC 212296912), *TESS* collected data in sectors 1 (2018 July 25–August 22) and 27 (2020 July 4–July 30). In this case, we did not consider the data between either 2458347.2 and 2458349.4 or 2458353.0 and 2458354.0 BJD, due to the presence of notorious uncorrected systematics, and we discarded all sector 27 data because of the inclusion of flux coming from another object in the light curve. We searched for periodic modulations in the time-series observations by running a Lomb–Scargle (LS) periodogram (Scargle 1982) provided by the ASTROPY package (Astropy Collaboration 2013). For HD 29992, we found $P_{\rm rot} = 0.8669 \pm 0.0013$ days, with an amplitude[9] $A = 2.17 \times 10^{-4}$ mag, whilst for HD 196385 the period detected

---

[9]The amplitude of the variation was computed as $\sqrt{A_{\rm sin}^2 + A_{\rm cos}^2}$, where $A_{\rm sin}$ and $A_{\rm cos}$ are the amplitudes of the sine and cosine terms of the best model found by the LS periodogram.
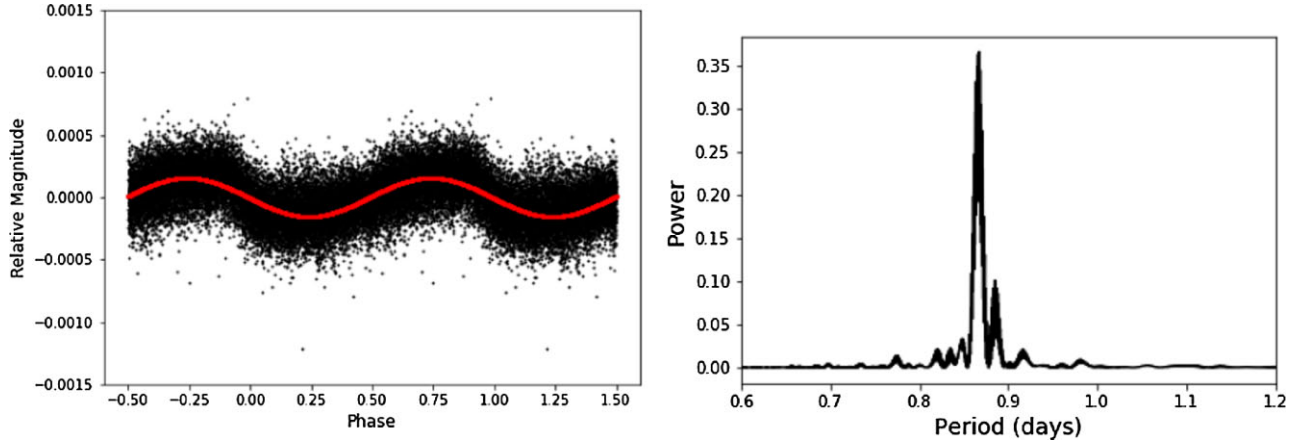
Figure A1. Left: *TESS* phase-folded light curve of HD 29992. Black crosses indicate the unbinned *TESS* PDC_SAP data, and the red continuous line points out the model corresponding to the best period detected. Right: LS periodogram.

Figure A2. Left: *TESS* phase-folded light curve of HD 196385. Black crosses indicate the unbinned *TESS* PDC_SAP data, and the red continuous line points out the model corresponding to the best period detected. Right: LS periodogram.
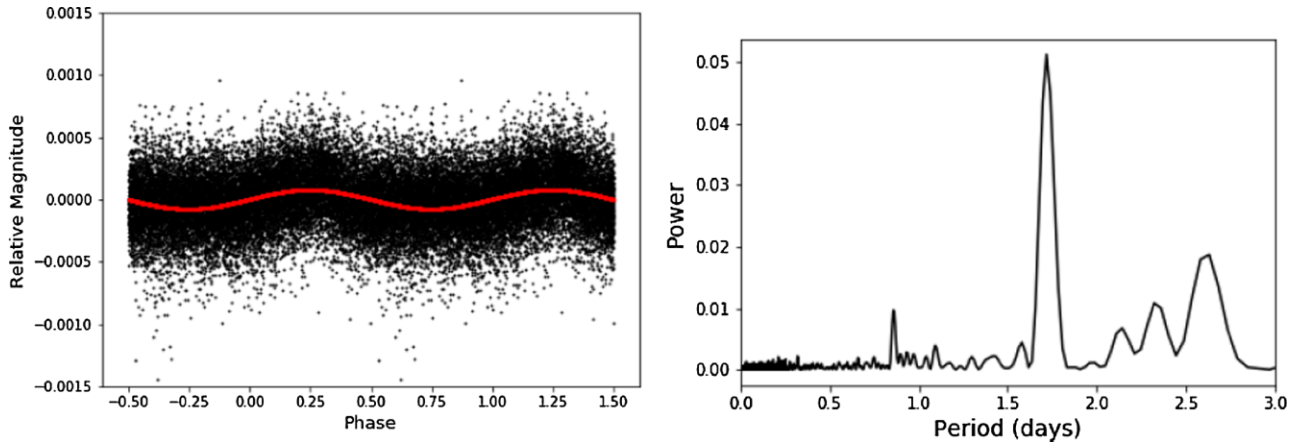
was $P_{\rm rot} = 1.7178 \pm 0.0361$ days, with an amplitude $A = 7.7 \times 10^{-5}$ mag. *TESS* phase-folded data and LS periodograms for both stars are shown in Figs A1 and A2. Finally, we superimposed the *TESS* fields and the adopted apertures for HD 29992 and HD 196385 over the location of nearby *Gaia* DR2 sources. The fact that no *Gaia* sources, with a difference in magnitude relative to the star of interest smaller than 8, fell inside or in the surroundings of the selected apertures would indicate that the origin of the signal effectively comes from the sources under study. Moreover, none of the Data Release Notes of the sectors analysed reported additional periodic systematics that might mimic the peaks found by LS. All these considerations lead us to suggest with high confidence that the periodic signals found have an astrophysical origin and come from the targets analysed in this work. As far as we are aware, this would be the first time that photometric rotation periods have been reported for these stars. In order to check whether the rotation rates are consistent with the ages presented in Table 1, we used gyrochronology (Barnes 2007). This technique relates the stellar rotation period $P_{\rm rot}$ to the age t and the colour $(B - V)_0$ by the formula $P_{\rm rot} = t^n \times a[(B - V)_0 - c]^b$, where a, b, and c are known as the gyrochronology parameters. Recently, Chowdhury et al. (2018) analysed 15 106 A–K stars observed by the *Kepler* satellite and showed that this relationship can be extended to colours $(B - V)_0$ down to 0.2 by considering different values of the parameter

c. In this work, we adopted $a = 0.77$ and $b = 0.55$ from Meibom, Mathieu & Stassun (2009), $n = 0.5$ following Skumanich (1972), and $c = 0.36$ and 0.3 for HD 29992 and HD 196385, respectively, as arbitrarily selected in Chowdhury et al. (2018). Colours $(B - V)_0$ were calculated as the difference between the values of B and V magnitudes extracted from SIMBAD. We obtained $(B - V)_0 = 0.37$ for HD 29992 and $(B - V)_0 = 0.307$ for HD 196385. Using all this information, we computed gyrochronology ages of 1.17 and 0.2 Gyr for HD 196385 and HD 29992, respectively. For the first star, this value is, within errors, in good agreement with the age of Table 1. For HD 29992, although the age obtained from gyrochronolgy is not within the uncertainty of that derived by Casagrande et al. (2011), it differs by only 1.5 Gyr.

Stellar radii of $R_\star = 1.89 \pm 1.80$ R$_\odot$ for HD 29992 and $R_\star = 1.51 \pm 1.46$ R$_\odot$ for HD 196385 were extracted from the *Gaia* DR2 catalogue (Gaia Collaboration et al. 2016, 2018), and rotational velocities of $v \sin(i_\star) = 100$ km s^{-1} and $v \sin(i_\star) = 13$ km s^{-1} were taken from the work of Borgniet et al. (2017). We introduced these values and the rotation periods estimated from the *TESS* data in equation (A1) and obtained inclinations of $i_\star = 65.3°$ for HD 29992 and $i_\star = 16.9°$ for HD 196385.

This paper has been typeset from a TEX/LATEX file prepared by the author.